

Dalton Transactions

Accepted Manuscript



This is an *Accepted Manuscript*, which has been through the Royal Society of Chemistry peer review process and has been accepted for publication.

Accepted Manuscripts are published online shortly after acceptance, before technical editing, formatting and proof reading. Using this free service, authors can make their results available to the community, in citable form, before we publish the edited article. We will replace this *Accepted Manuscript* with the edited and formatted *Advance Article* as soon as it is available.

You can find more information about *Accepted Manuscripts* in the [Information for Authors](#).

Please note that technical editing may introduce minor changes to the text and/or graphics, which may alter content. The journal's standard [Terms & Conditions](#) and the [Ethical guidelines](#) still apply. In no event shall the Royal Society of Chemistry be held responsible for any errors or omissions in this *Accepted Manuscript* or any consequences arising from the use of any information it contains.

**Electronic and Phonon Transports in Sb-doped $\text{Ti}_{0.1}\text{Zr}_{0.9}\text{Ni}_{1+x}\text{Sn}_{0.975}\text{Sb}_{0.025}$
Nanocomposites**

Yuanfeng Liu¹, Alexander Page², Pranati Sahoo¹, Hang Chi², Ctirad Uher² and Pierre F. P. Poudeu^{1,*}

1) Laboratory for Emerging Energy and Electronic Materials, Department of Materials Science and Engineering, University of Michigan, Ann Arbor, 48109, USA

2) Department of Physics, University of Michigan, Ann Arbor, MI, 48109, USA

*Corresponding author. Tel: +1-734-763-8436; Fax: +1-734-763-4788

Email: ppoudeup@umich.edu (PFPP)

Keywords: Keywords: Nanostructures • Energy Filtering • Heavily-doped Semiconductor • Half-Heusler/Full-Heusler • Thermoelectrics

RECEIVED DATE

Abstract

The thermoelectric behavior of n-type Sb-doped half-Heusler (HH) – full-Heusler (FH) nanocomposites with general composition $\text{Ti}_{0.1}\text{Zr}_{0.9}\text{Ni}_{1+x}\text{Sn}_{0.975}\text{Sb}_{0.025}$ ($x = 0, 0.02, 0.04, 0.1$) was investigated in the temperature range from 300 to 775K. Samples used for structural characterization and transport measurements were obtained through solid-state reaction of high purity elements at 950 °C and densification of the resulting polycrystalline powders using a uniaxial hot press. X-ray diffraction study of the powder samples suggested the formation of single-phase HH alloys regardless of the Ni concentration (x value). However, high resolution transmission electron microscopy investigation revealed the presence of spherical nanoprecipitates with a broad size distribution coherently embedded inside the HH matrix. The size range and dispersion of the precipitates depend on the concentration of Ni in the starting mixture. Well dispersed nanoprecipitates with size ranging from 5 nm to 50 nm are observed in the nanocomposite with $x = 0.04$, while severe agglomeration of large precipitates (>50 nm) is observed in samples with $x = 0.1$. Hall Effect measurements of various samples indicate the carrier concentration within the Sb-doped HH matrix remains nearly constant ($\sim 7 \times 10^{20} \text{ cm}^{-3}$) for samples with $x = 0.02$ and $x = 0.04$, whereas a significant increase of the carrier concentration to $\sim 9 \times 10^{20} \text{ cm}^{-3}$ is observed for the sample with $x = 0.1$. Interestingly, only a marginal change in thermopower value is observed for various samples despite the large difference in the carrier density. In addition, the carrier mobility remains constant up to $x = 0.04$ suggesting that the small nanoprecipitates in these samples do not disrupt electronic transport within the matrix. Remarkably, a large reduction in the total thermal conductivity is observed for all nanocomposites, indicating the effectiveness of the embedded nanoprecipitates in scattering phonons while enabling efficient electron transfer across the matrix/inclusion interfaces.

Introduction

Nanostructuring of bulk semiconductors through insertion of additional phases with various length scales within the semiconducting matrix has been widely demonstrated as an effective method to achieve a large increase in the overall figure of merit, $ZT = \sigma S^2 T / \kappa$, (where σ is the electric conductivity, S is the thermopower, T is the absolute temperature and κ is the thermal conductivity) of the resulting nanocomposites¹⁻⁵. The observed large ZT values are often credited to drastic reduction in the total thermal conductivity arising from the scattering of a broad phonon spectrum at matrix/nano-inclusions interfaces and at grain boundaries with various length scales⁵⁻¹⁶. However, the high density of interfaces (phase boundaries and grain boundaries) within the semiconducting matrix arising from the nanostructuring generally leads to large reductions in the carrier mobility offsetting the benefit of the large reduction in total thermal conductivity. Recently, the concept of band-engineering at the matrix-nano-inclusions interfaces has been introduced as an effective strategy to achieve efficient electronic transport simultaneously with large reductions of the lattice thermal conductivity in bulk nanostructured semiconductors^{5, 15-19}. This concept exploits structural similarities between the matrix and inclusion phases to create matrix/inclusion interfaces with arrangement (alignment or offset) of their valence band (VB) and/or conduction band (CB) favorable to efficient carrier transport. For instance, a small mismatch between unit cell dimensions is necessary to achieve the formation of coherent matrix/inclusion phase boundaries, while a similarity in the positional distribution of at least one type of atom within both structures (matrix and inclusion) is expected to increase the degree of similarity between the electronic band structure of both phases facilitating their suitable arrangement at their interface. Minimal disruption of the electronic transport and in few cases even some enhancements in the carrier mobility and thermopower, have been reported in such bulk nanostructured materials^{1, 2, 5, 14-27}. For example, we have recently observed that large enhancements in the carrier mobility and thermopower can be achieved simultaneously with large reductions in the thermal conductivity in both n-type and p-type half-Heusler alloys when nanometer scale full-Heusler nanostructures are coherently embedded within their matrices^{17-19, 28}.

HH (TMX) and FH (TM₂X) alloys are intermetallic compounds with closely related crystal structures. For a selected combination of the elements T, M and X (T and M are transition or rare-earth metals, and X is a main-group element), one can generate the FH structure (MnCu₂Al structure-type; Fm-3m) from that of HH (MgAgAs structure type; F-43m), which consists of four interpenetrating face-centered cubic (*fcc*) sublattices of T (0,0,0); M (1/4, 1/4, 1/4); X (1/2, 1/2, 1/2); and vacancy (3/4, 3/4, 3/4), by insertion of additional X atoms into the vacant position in the HH structure. Therefore, it is anticipated that coherent HH/FH phase boundaries arising from small lattice mismatch and band alignment at the HH/FH interfaces will form and produce favorable efficient electronic transport properties due to the similarity in the packing of T and X atoms in both HH and FH structures. The additional X atom creates a partially filled band with X character on top of the HH valence band (VB), which pushes the valence band maxima (VBM) and the conduction band minima of the FH phase to higher energy¹⁷. Our early investigation of the electronic transports in (1-x)(Ti_{0.1}Zr_{0.9})NiSn(HH)/(x)(Ti_{0.1}Zr_{0.9})Ni₂Sn(FH)¹⁷ and (1-x) Zr_{0.25}Hf_{0.75}NiSn(HH)/(x)Zr_{0.25}Hf_{0.75}Ni₂Sn(FH)¹⁸ systems revealed a large increase in the thermopower and carrier mobility simultaneously with large reductions in the total thermal conductivity for nanocomposites containing well dispersed nanometer scale (FH) inclusions coherently embedded in the HH matrix. However, large reductions in the thermopower and carrier mobility, and large increases in the electrical conductivity and thermal conductivity was also obtained in (1-x)Zr_{0.25}Hf_{0.75}NiSn(HH)/(x)Zr_{0.25}Hf_{0.75}Ni₂Sn(FH) when the FH nanoinclusions agglomerate into large clusters inside the HH matrix²⁸, suggesting a strong correlation between the average size the FH inclusions and their contribution to the electronic transport in the HH/FH composites. Large increases in the overall carrier density with increasing FH content was obtained for HH/FH nanocomposites containing large FH inclusions²⁸, whereas gradual reductions in the effective carrier density with increasing FH content was observed when the average size of the FH inclusion is sufficiently small¹⁷⁻¹⁸. This reduction of the effective carrier density was attributed to the trapping of low energy carriers and the HH/FH interfacial potential (ΔE) arising from the offset of the CB and VB in both HH and FH structures¹⁷.

In this work, we explore the effect of the HH/FH interfacial potential, ΔE , on the electronic transport in heavily doped $\text{Ti}_{0.1}\text{Zr}_{0.9}\text{Ni}_{1+x}\text{Sn}_{0.975}\text{Sb}_{0.025}$ ($x = 0, 0.02, 0.04, 0.1$) nanocomposites. The formation of the FH nanoinclusions within the HH matrix was confirmed by high resolution transmission electron microscopy (HRTEM) studies. We found that the substitution of Sn by 2.5% Sb results in large increases of the carrier density from $\sim 6 \times 10^{19} \text{ cm}^{-3}$ ($\text{Ti}_{0.1}\text{Zr}_{0.9}\text{NiSn}^{17}$) to $\sim 6 \times 10^{20} \text{ cm}^{-3}$ ($\text{Ti}_{0.1}\text{Zr}_{0.9}\text{NiSn}_{0.975}\text{Sb}_{0.025}$). The formation FH precipitates in the Sb-doped $\text{Ti}_{0.1}\text{Zr}_{0.9}\text{NiSn}_{0.975}\text{Sb}_{0.025}$ matrix maintains the carrier density nearly constant for composition with $x = 0.02$ and 0.04 where a large fraction of the FH inclusions are small ($< 20 \text{ nm}$) and well dispersed, whereas the clustering for FH inclusions into large particles (20 nm to 100 nm) in the sample with $x = 0.1$, resulted in a large increase of the carrier density to $\sim 9 \times 10^{20} \text{ cm}^{-3}$. Surprisingly, only a marginal change is observed on the thermopower and electrical conductivity of all $\text{Ti}_{0.1}\text{Zr}_{0.9}\text{Ni}_{1+x}\text{Sn}_{0.975}\text{Sb}_{0.025}$ ($x = 0, 0.02, 0.04, 0.1$) samples despite the large increase in the carrier density observed for the sample with $x = 0.1$. It is remarkable to note that the carrier mobility in the samples with $x = 0.02$ and 0.04 is very similar to the carrier mobility of the matrix. The observed constant values of the thermopower and electrical conductivity for various $\text{Ti}_{0.1}\text{Zr}_{0.9}\text{Ni}_{1+x}\text{Sn}_{0.975}\text{Sb}_{0.025}$ ($x = 0, 0.02, 0.04, 0.1$) samples suggests that nanostructuring through coherent insertion of FH inclusions within the HH matrix does not disrupt electronic transport resulting in a constant power factor (PF) for various samples. Interestingly, a reduction in the thermal conductivity was observed for various nanocomposites when compared to the Sb-doped HH matrix. These results clearly suggest that band-engineering through atomic-scale engineering of the structure and chemistry of the matrix-inclusion interfaces is an efficient strategy to achieve large reductions in the thermal conductivity of the semiconducting matrix with minimal disruption of its electronic transports.

Experimental

Synthesis. The Sb-doped HH(1-x)/FH(x) nanocomposites with general compositions $\text{Ti}_{0.1}\text{Zr}_{0.9}\text{Ni}_{1+x}\text{Sn}_{0.975}\text{Sb}_{0.025}$ ($x = 0, 0.02, 0.04, 0.1$) used in this study were synthesized by solid state reaction of high purity (99.99%) elemental powders (Ti, Zr, Ni, Sn and Sb) in the desired ratio. The starting mixtures containing various fractions of Ni were

thoroughly ground under Ar atmosphere in a glove-box using an agate mortar and pestle. Then, the activated powder was sealed in a quartz tube under a residual pressure of 10^{-4} Torr and heated sequentially to 300 °C for 3 days and to 900 °C and 7 days. The resulting products were consolidated into pellets at 950 °C under and applied pressure of 100 MPa using our uniaxial hot press system. Detailed densification procedures are described elsewhere^{18, 25, 28} The relative densities of the pressed pellets were obtained by dividing the geometrical density (calculated using the pellet's dimension and mass) by the “true” density of the as-synthesized polycrystalline powder, measured using He gas pycnometry on a Quantachrome Micro Ultrapyc 1200e. The relative density of all hot pressed pellets was above 98%.

Characterization. The structure and phase purity of the as-prepared polycrystalline powders were investigated using powder X-ray diffraction on a rotating anode Rigaku powder diffractometer operating under 40 kV and 40 mA using a monochromated Cu $K\alpha$ radiation. The internal structure of selected specimens cut from pressed pellets was investigated by high resolution transmission electron microscopy (HRTEM) using JEOL 3011 to probe the size and the distribution of FH nanoinclusions embedded within the HH matrix as well as the interface boundary between HH and FH phases. Details on TEM sample preparation are described elsewhere^{18, 25, 28}. Thermopower and electrical resistivity were measured simultaneously from room temperature to 500 °C under a low pressure He atmosphere using a commercial ZEM-3 system from ULVAC-RIKO. The instrument precision on the electrical resistivity and thermopower is $\pm 4\%$. The thermal conductivity was calculated from the thermal diffusivity data measured by the laser flash method (LFA-1000 from Linseis) from 20 °C to 500 °C under dynamic vacuum ($\sim 10^{-3}$ Torr). The instrument precision on the thermal diffusivity data is $\pm 3\%$. The Hall coefficients data were measured in the temperature range from 300 K to 775K under the magnetic field of 1T using a large Oxford air-bore superconducting magnet cryostat that accommodates a small tubular oven and a Hall insert. The instrument uncertainty on Hall coefficient data is $\pm 5\%$. The electrical conductivity data were combined with the Hall coefficient measurements to evaluate and extract accurate information on the temperature dependence of the carrier density and the mobility of the charge carriers in the nanocomposites.

Results and analysis

Crystal structure and microstructure. Careful analysis of the X-ray diffraction patterns (Fig 1A) of the synthesized $\text{Ti}_{0.1}\text{Zr}_{0.9}\text{Ni}_{1+x}\text{Sn}_{0.975}\text{Sb}_{0.025}$ ($x = 0, 0.02, 0.04, 0.1$) suggested the formation of single phase HH alloys.

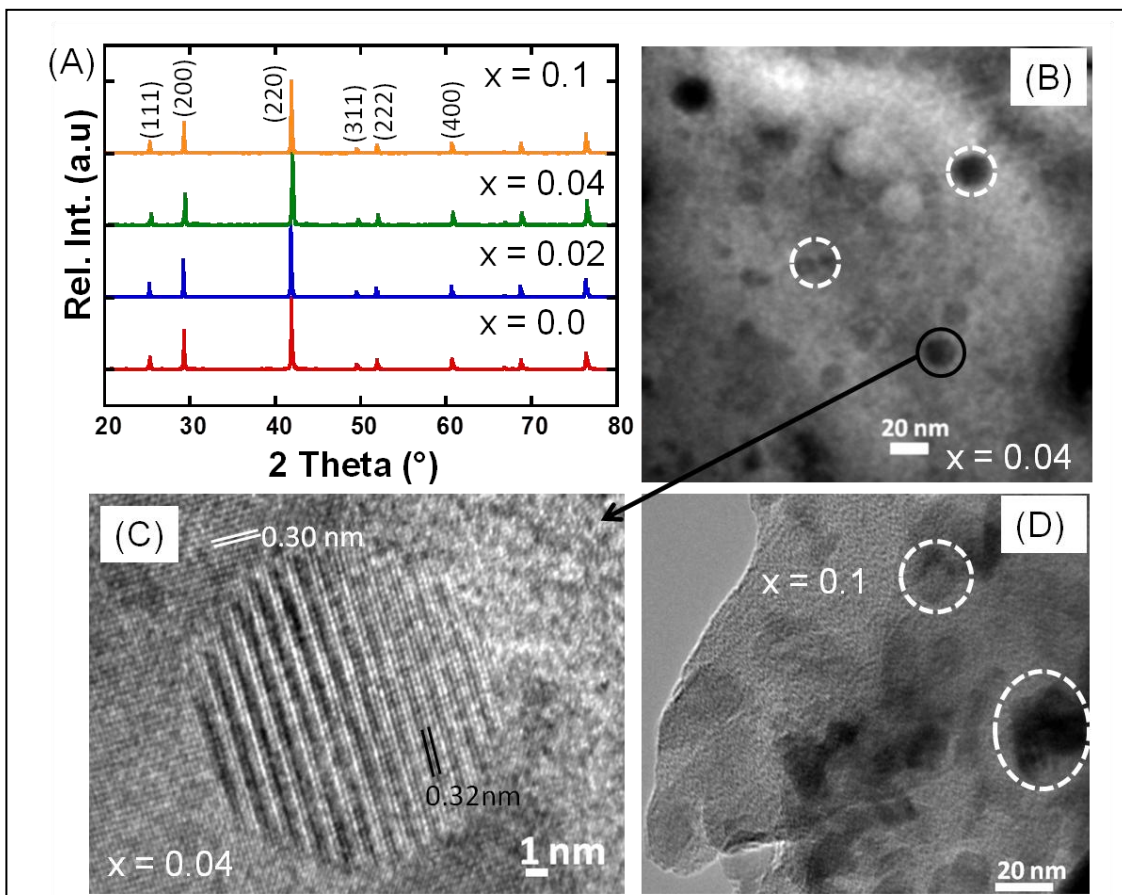


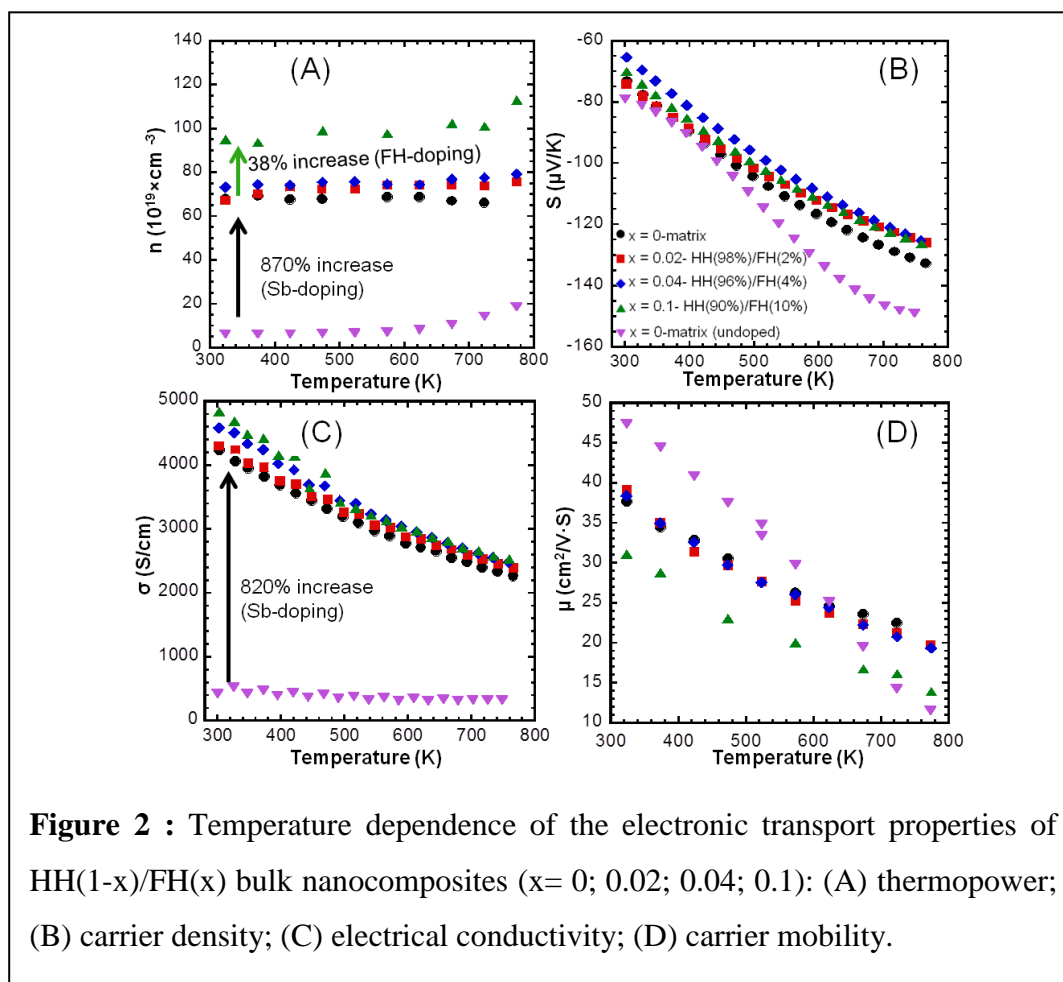
Figure 1: Structural characteristic of $\text{Ti}_{0.1}\text{Zr}_{0.9}\text{Ni}_{1+x}\text{Sn}_{0.975}\text{Sb}_{0.025}$ ($x = 0, 0.02, 0.04, 0.1$) nanocomposites. (A) Powder X-ray diffraction patterns showing only peaks corresponding to the HH matrix. (B) Low magnification TEM image of the sample with $x = 0.04$, revealing the presence of spherical FH precipitates embedded in the HH matrix. (C) High magnification image of a typical FH nanostructure from the sample with $x = 0.04$ showing the highly coherent phase boundary with the surrounding HH matrix. (D) Low magnification TEM image of the sample with $x = 0.1$ showing high agglomeration of FH nanostructures into large particles.

All diffraction peaks were indexed in the cubic MgAgAs structure type (space group: $F-43m$). No additional peak that could be assigned to the anticipated FH secondary phase or

to any other impurity phase could be observed on the diffractions patterns, even for samples with the expected FH mole fraction of up to 10% ($x = 0.1$). This suggests that the excess elemental Ni added in the starting mixture is dissolved into interstitial sites in the structure of the HH matrix to form interstitial solid-solution or are located on the vacant (3/4, 3/4, 3/4) site in the HH structure to form FH phases that are too small to strongly diffract X-ray radiation. In the event of the formation of interstitial solid-solution, one should observe a gradual increase in the unit cell parameter of the HH matrix with increasing excess Ni (x value). However, the refinement of the unit cell parameter of the HH phase in various $\text{Ti}_{0.1}\text{Zr}_{0.9}\text{Ni}_{1+x}\text{Sn}_{0.975}\text{Sb}_{0.025}$ ($x = 0, 0.02, 0.04$ and 0.1) compositions using diffraction peaks from the XRD patterns showed a constant value ($a \sim 6.096(2) \text{ \AA}$) for all samples suggesting that interstitial solid-solution between HH and excess elemental Ni is unlikely. To investigate the anticipated formation of small precipitates in various $\text{Ti}_{0.1}\text{Zr}_{0.9}\text{Ni}_{1+x}\text{Sn}_{0.975}\text{Sb}_{0.025}$ ($x = 0.02, 0.04$ and 0.1) samples and to characterize their morphology, average size and dispersion, high resolution transmission electron microscopy (HRTEM) study was carried out on selected specimens. A low magnification TEM image of the sample with $x = 0.04$ is shown in Figure 1B. It can be seen clearly that spherical precipitates of the FH phase with size ranging from $< 5 \text{ nm}$ to 20 nm are well dispersed within the HH matrix. These FH precipitates are coherently embedded within the HH matrix (Fig.1C) as no obvious strained domain could be observed at the matrix/ inclusion interface. The spacing between neighboring lattice planes in the HH matrix and FH inclusions are $\sim 0.30 \text{ nm}$ and $\sim 0.32 \text{ nm}$, respectively. This indicates a coherent alignment of the (200) planes of the HH matrix and FH inclusion at the matrix/inclusion interfaces. The observed coherent phase boundaries between the matrix and inclusion phases (Fig. 1C) are expected to promote charge carrier transfer across the matrix/inclusion interfaces. Increasing the concentration of excess Ni to $x = 0.1$ resulted in the precipitation and agglomeration of the FH nanophase into large particles with size ranging from 20 nm to 100 nm (Fig. 1D).

Thermoelectric properties. The temperature dependence of the electronic transport properties of the synthesized $\text{Ti}_{0.1}\text{Zr}_{0.9}\text{Ni}_{1+x}\text{Sn}_{0.975}\text{Sb}_{0.025}$ ($x = 0, 0.02, 0.04, 0.1$), HH(1- x)/FH(x) bulk nanocomposites is shown in Figure 2. At 300K the carrier density of the

Sb-doped $\text{Ti}_{0.1}\text{Zr}_{0.9}\text{NiSn}_{0.975}\text{Sb}_{0.025}$ HH matrix is $\sim 6.8 \times 10^{20} \text{ cm}^{-3}$, (Fig.2A) which corresponds to 870% increase compared to the carrier density measured on the undoped $\text{Ti}_{0.1}\text{Zr}_{0.9}\text{NiSn}$ sample¹⁷. This is consistent with the expected increase in the density of electrons upon substituting 2.5% Sn by Sb in $\text{Ti}_{0.1}\text{Zr}_{0.9}\text{NiSn}$. The carrier density remains constant in $\text{Ti}_{0.1}\text{Zr}_{0.9}\text{Ni}_{1+x}\text{Sn}_{0.975}\text{Sb}_{0.025}$ nanocomposites with $x = 0.02$ (HH(98%)/FH (2%)) and $x = 0.04$ (HH(96%)/FH(4%)). This suggests that the FH nanostructures incorporated in the HH (98%)/FH (2%) and HH (96%)/FH (4%) samples are not electronically active. However, increasing the concentration of excess Ni to $x = 0.1$ (HH(90%)/FH(10%)) resulted in a 38% increase ($\sim 9.4 \times 10^{20} \text{ cm}^{-3}$) in the carrier density when compared to the Sb-doped matrix. This increase in the carrier density is attributed to electronic doping of the HH matrix by the FH inclusions. Regardless of the x values, the carrier density remains nearly constant with increasing temperature, indicating that

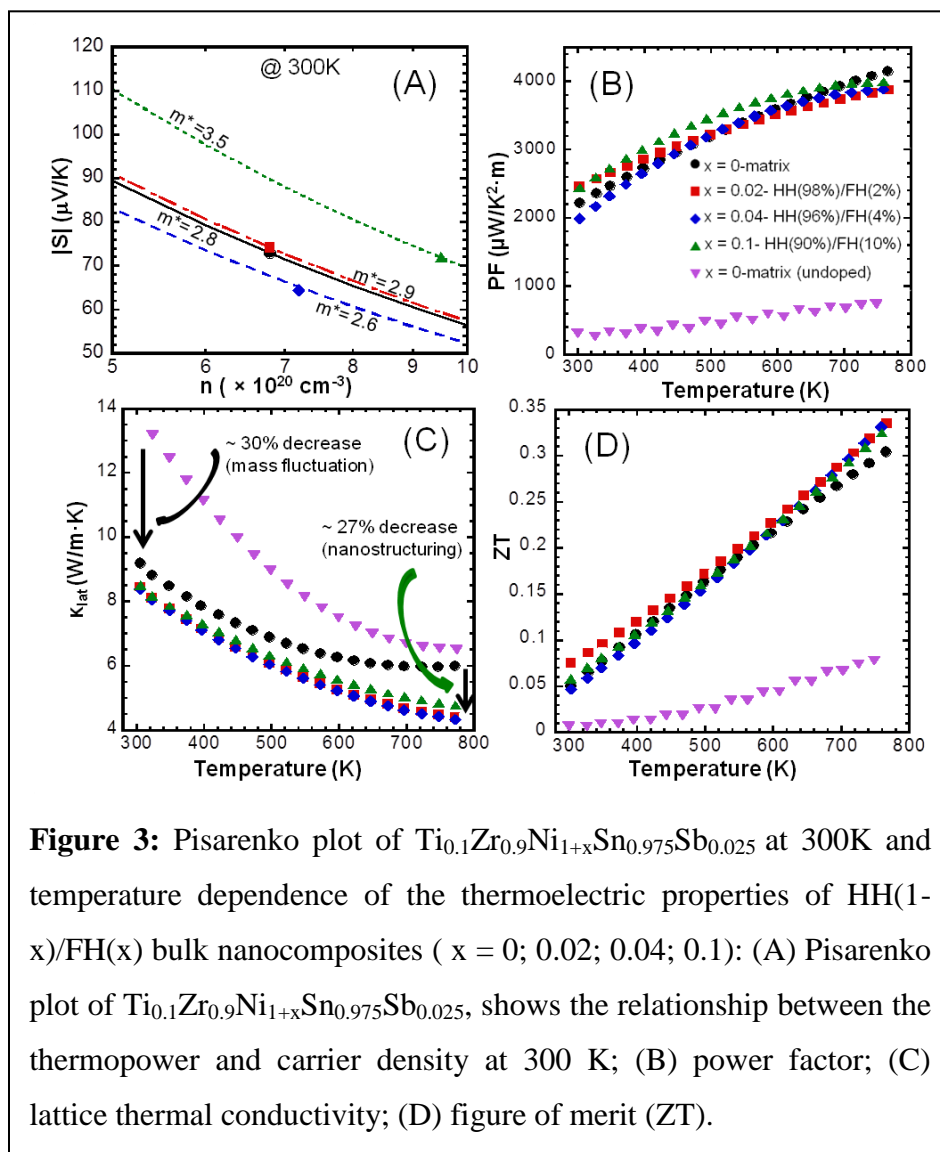


the synthesized samples are heavily doped semiconductors.

To better understand the observed difference in the alteration of the carrier density by the FH inclusions in HH(98%)/FH(2%), HH(96%)/FH(4%) and HH(90%)/FH(10%), one must take into consideration the microstructures of various samples. TEM images of the HH(96%)/FH(4%) and (HH(90%)/FH(10%) samples showed that a large fraction of the FH inclusions in HH(96%)/FH(4%) are smaller than 20 nm and are well dispersed, whereas in HH(90%)/FH(10%) sample, the FH inclusions agglomerate in to large particles (Figs. 1B and 1D). Considering that the FH phase in bulk form is metallic, one would anticipate a gradual increase in the carrier density with increasing mole fraction of FH inclusions in various HH(1-x)/FH(x) samples due to electronic doping of the semiconducting HH matrix by the FH inclusions. Therefore, the constant carrier density observed in the HH(98%)/FH(2%) and HH(96%)/FH(4%) samples indicates that small (< 20 nm) FH inclusions are likely insulating or semiconducting and upon agglomeration into large (> 20nm) particles (Fig. 1D), the bulk metallic character of the FH phases is recovered. This analysis is consistent with results from our previous investigations in comparable systems^{17, 18, 28}.

Figure 2B shows the temperature dependence of the thermopower in the synthesized $\text{Ti}_{0.1}\text{Zr}_{0.9}\text{Ni}_{1+x}\text{Sn}_{0.975}\text{Sb}_{0.025}$ nanocomposites. All samples show negative values of the thermopower in the whole temperature range indicating n-type semiconducting behavior. At 300K the thermopower of the sample with $x = 0$ (Sb-doped matrix) is $\sim -74 \mu\text{V/K}$, which is very similar to the value ($\sim -78 \mu\text{V/K}$) measured for the undoped $\text{Ti}_{0.1}\text{Zr}_{0.9}\text{NiSn}$ matrix¹⁷. Surprisingly, the thermopower at 300K of various $\text{Ti}_{0.1}\text{Zr}_{0.9}\text{Ni}_{1+x}\text{Sn}_{0.975}\text{Sb}_{0.025}$ nanocomposites remains nearly constant with increasing x values, despite the 38% increase in the carrier density obtained for the sample with $x = 0.1$. Regardless of the composition, the absolute values of the thermopower of $\text{Ti}_{0.1}\text{Zr}_{0.9}\text{Ni}_{1+x}\text{Sn}_{0.975}\text{Sb}_{0.025}$ nanocomposites increase with rising temperature reaching a value of $\sim -130 \mu\text{V/K}$ at 775K. The observed similar values of the thermopower of $\text{Ti}_{0.1}\text{Zr}_{0.9}\text{Ni}_{1+x}\text{Sn}_{0.975}\text{Sb}_{0.025}$ samples despite the difference in the carrier density for the sample with $x = 0.1$ can be explained by the change in the carrier effective mass (m^*). From the Pisarenko plots (Fig. 3A) describing the relationship between the thermopower and carrier density for each of the $\text{Ti}_{0.1}\text{Zr}_{0.9}\text{Ni}_{1+x}\text{Sn}_{0.975}\text{Sb}_{0.025}$ samples at 300K, $S =$

$[(8\pi^2(k_B)^2)/3eh^2]m^*T(\pi/3n)^{2/3}$ (k_B is the Boltzmann constant, e is the carrier charge, h is the Planck's constant, m^* is the effective mass of the charge carrier, T is the absolute temperature, n is the carrier density)²⁹, we observed that the high carrier density of the sample with $x = 0.1$ is compensated by an increase in the carrier effective mass $m^* = 3.5 m_e$.



The temperature dependence of the electrical conductivity of the synthesized $\text{Ti}_{0.1}\text{Zr}_{0.9}\text{Ni}_{1+x}\text{Sn}_{0.975}\text{Sb}_{0.025}$ nanocomposites is shown in Figure 2C. At 300K the $\text{Ti}_{0.1}\text{Zr}_{0.9}\text{Ni}_{1+x}\text{Sn}_{0.975}\text{Sb}_{0.025}$ ($x = 0$) matrix displays a large electrical conductivity, ~ 4200 S/cm. This corresponds to $\sim 820\%$ increase when compared to the electrical conductivity

of undoped $\text{Ti}_{0.1}\text{Zr}_{0.9}\text{NiSn}$ matrix¹⁷. The observed electrical conductivity is consistent with the large increase in the carrier density arising from the partial substitution of 2.5% Sn by Sb in $\text{Ti}_{0.1}\text{Zr}_{0.9}\text{NiSn}$. The electrical conductivity decreases with increasing temperature, which is consistent with heavily doped semiconducting behavior. Regardless of the x values (fraction of FH inclusions), the electrical conductivities of all $\text{Ti}_{0.1}\text{Zr}_{0.9}\text{Ni}_{1+x}\text{Sn}_{0.975}\text{Sb}_{0.025}$ nanocomposites remain nearly constant in the temperature range investigated. The observed comparable values of the electrical conductivities of the samples with $x = 0, 0.02$ and 0.04 resulted from the similarity in their carrier density and mobility (Fig. 2D), whereas for the sample with $x = 0.1$, the large increase in the carrier density (Fig. 2A) is compensated by a decrease in the carrier mobility. The observed constant carrier mobility in $\text{Ti}_{0.1}\text{Zr}_{0.9}\text{Ni}_{1+x}\text{Sn}_{0.975}\text{Sb}_{0.025}$ nanocomposites with $x = 0.02$ and 0.04 is quite surprising and suggests that the embedded FH inclusions do not alter charge carriers transport at the HH/FH interfaces. The fitting of the temperature dependence of the carrier mobility of $\text{Ti}_{0.1}\text{Zr}_{0.9}\text{Ni}_{1+x}\text{Sn}_{0.975}\text{Sb}_{0.025}$ nanocomposites using the power law $T^{-\lambda}$ resulted in λ values of 0.81 ($x = 0$), 0.77 ($x = 0.02$), 0.74 ($x = 0.04$) and 0.94 ($x = 0.1$). The observed values of the power exponent λ suggest that the temperature dependence of the carrier mobility at high temperatures is affected by both acoustic phonon and optical phonon scattering.

Figure 3B shows the temperature dependence of the power factor ($\text{PF} = \sigma \cdot S^2$) of Sb-doped $\text{Ti}_{0.1}\text{Zr}_{0.9}\text{Ni}_{1+x}\text{Sn}_{0.975}\text{Sb}_{0.025}$ nanocomposites. At 300K the PF of the Sb-doped HH- matrix ($\text{Ti}_{0.1}\text{Zr}_{0.9}\text{NiSn}_{0.975}\text{Sb}_{0.025}$) is $\sim 2200 \mu\text{W}/\text{K}^2 \cdot \text{m}$. This value is six times larger than the value measured for the undoped HH-matrix ($\text{Ti}_{0.1}\text{Zr}_{0.9}\text{NiSn}$) and is consistent with the large increase in the electrical conductivity upon Sb doping at Sn sites in the structure of $\text{Ti}_{0.1}\text{Zr}_{0.9}\text{NiSn}$. The PF of the Sb-doped matrix increases monotonically with rising temperature reaching a value of $4000 \mu\text{W}/\text{K}^2 \cdot \text{m}$ at 775K. Interestingly, the insertion of various fractions of FH nanoinclusions in the Sb-doped HH-matrix ($\text{Ti}_{0.1}\text{Zr}_{0.9}\text{NiSn}_{0.975}\text{Sb}_{0.025}$) maintains the PF of resulting $\text{Ti}_{0.1}\text{Zr}_{0.9}\text{Ni}_{1+x}\text{Sn}_{0.975}\text{Sb}_{0.025}$ nanocomposites essentially unchanged at all temperatures (Fig. 3B). This result is consistent with the observed comparable values of the electrical conductivity and thermopower of various $\text{Ti}_{0.1}\text{Zr}_{0.9}\text{Ni}_{1+x}\text{Sn}_{0.975}\text{Sb}_{0.025}$ nanocomposites. It also suggests that the embedded FH nanoinclusions are electronically inert (i.e. do not significantly alter the

effective carrier density) with regards to the Sb-doped HH matrix and are transparent to charge carriers leading to marginal alteration of the carrier mobility at the HH/FH interfaces.

The temperature dependence of the lattice thermal conductivity of the synthesized Sb-doped $\text{Ti}_{0.1}\text{Zr}_{0.9}\text{Ni}_{1+x}\text{Sn}_{0.975}\text{Sb}_{0.025}$ nanocomposites is shown in Figure 3C. At 300K, the lattice thermal conductivity of the Sb-doped HH- matrix ($\text{Ti}_{0.1}\text{Zr}_{0.9}\text{NiSn}_{0.975}\text{Sb}_{0.025}$) is ~ 9 W/m·K. This corresponds to a 30% reduction from the lattice thermal conductivity of the undoped matrix ($\text{Ti}_{0.1}\text{Zr}_{0.9}\text{NiSn}$). The observed reduction in the lattice thermal conductivity of Sb-doped matrix at 300K is attributed to the scattering of phonon by mass fluctuation and point defects arising from the intermixing of Sn and Sb at various Sn sites in the structure of $\text{Ti}_{0.1}\text{Zr}_{0.9}\text{NiSn}$. Interestingly, additional reductions in the lattice thermal conductivity are obtained through the insertion of various fractions of FH nanoinclusions in the Sb-doped HH matrix. The lattice thermal conductivities of the Sb-doped $\text{Ti}_{0.1}\text{Zr}_{0.9}\text{Ni}_{1+x}\text{Sn}_{0.975}\text{Sb}_{0.025}$ nanocomposites decrease with increasing temperature reaching a value of 4.4 W/m·K at 775K for the sample with $x = 0.04$. This corresponds to 27% reduction when compared to the lattice thermal conductivity of the Sb-doped HH matrix ($\text{Ti}_{0.1}\text{Zr}_{0.9}\text{NiSn}_{0.975}\text{Sb}_{0.025}$) at 775K. We attribute the observed large reductions in the lattice thermal conductivity of $\text{Ti}_{0.1}\text{Zr}_{0.9}\text{Ni}_{1+x}\text{Sn}_{0.975}\text{Sb}_{0.025}$ nanocomposites at high temperatures to enhanced phonon scattering at multiple HH/FH coherent interfaces dispersed throughout the Sb-doped HH matrix.

Figure 3D shows the temperature dependence of the figure of merit, ZT, of various $\text{Ti}_{0.1}\text{Zr}_{0.9}\text{Ni}_{1+x}\text{Sn}_{0.975}\text{Sb}_{0.025}$ nanocomposites. The ZT value of ~ 0.05 was obtained at 300K for the Sb-doped HH matrix. However, upon increasing the temperature, the ZT values of the sample rapidly increase to ~ 0.3 at 775 K. This value is four times higher than the ZT ~ 0.08 measured for undoped HH matrix. The observed increase in the ZT is due to the optimization of the electronic properties through Sb doping at Sn sites in the structure of $\text{Ti}_{0.1}\text{Zr}_{0.9}\text{NiSn}$. The reduction in the lattice thermal conductivity of Sb-doped HH matrix, while maintaining the PF essentially unchanged achieved by introduction of coherent FH inclusions within the $\text{Ti}_{0.1}\text{Zr}_{0.9}\text{NiSn}_{0.975}\text{Sb}_{0.025}$ matrix resulted in an additional 13% increase in the overall ZT of the $\text{Ti}_{0.1}\text{Zr}_{0.9}\text{Ni}_{1+x}\text{Sn}_{0.975}\text{Sb}_{0.025}$ nanocomposites.

Conclusion

In summary, we have demonstrated the ability to combine in a HH semiconducting matrix with a given chemical composition, a large enhancement in the electronic properties (electrical conductivity and thermopower) using substitutional chemistry (Sb doping) with a significant reduction in the thermal conductivity via nanostructuring to drastically increase the figure of merit of the resulting HH nanocomposites. The key to this interesting independent manipulation of the power factor and lattice thermal conductivity of heavily doped HH(1-x)/FH(x) nanocomposites lies in the unique possibility of HH and FH compounds with similar chemical composition to form structurally coherent phase boundaries and suitable alignment of their valence bands and conduction bands at the HH/FH interfaces. These essential structural and electronic features of the HH/FH interfaces enable efficient carrier transfer across, while blocking the propagation of thermal phonon. From our earlier work on undoped $\text{Ti}_{0.1}\text{Zr}_{0.9}\text{NiSn}$ HH matrix, we found that the introduction of coherent FH nanoinclusions resulted in large decreases in the effective carrier density due to the filtering of low energy carriers at the HH/FH interfacial potential energy¹⁷. As a consequence, large increase in the thermopower and carrier mobility was observed for the resulting HH/FH nanocomposites simultaneously with large reductions in the lattice thermal conductivity. However, results from the current study show that under heavily doped conditions where the electronic conduction is likely controlled by a large fraction of extrinsic carriers with energy higher than the potential barrier at the HH/FH interfaces, the effect of filtering of low energy intrinsic carriers at the HH/FH interfaces on the overall carrier density of the sample is marginal. As a consequence, the thermopower and carrier mobility remain unchanged upon introduction of coherent FH nanoinclusions in a heavily doped semiconducting HH matrix. This explains the observed constant value of the PF for samples with various fractions of FH inclusions. It derives from the present work that one can efficiently reduce the thermal conductivity of heavily doped HH semiconductor using coherent FH nanostructures with marginal alteration of the PF. Such strategy can be easily applied to optimized HH matrices to further increase their thermoelectric figure of merit.

Acknowledgements

P.F.P.P. and C.U. gratefully acknowledge financial support from the Department of Energy, Office of Basic Energy Sciences under Award # DE-SC-0008574. This work made use of the TEM from the University of Michigan's Electron Microbeam Analysis Laboratory (EMAL), purchased with funds from the National Science Foundation Awards DMR-0315633 and DMR-0723032.

Reference

1. Ahn, K., et al., Enhanced thermoelectric properties of p-type nanostructured PbTe-MTe (M = Cd, Hg) materials. *Energy & Environmental Science*, 2013. **6**(5): p. 1529-1537.
2. He, J.Q., M.G. Kanatzidis, and V.P. Dravid, High performance bulk thermoelectrics via a panoscopic approach. *Materials Today*, 2013. **16**(5): p. 166-176.
3. Snyder, G.J. and E.S. Toberer, Complex thermoelectric materials. *Nature Materials*, 2008. **7**(2): p. 105-114.
4. Rowe, D.M., *CRC handbook of thermoelectrics*. 2010: CRC press.
5. Biswas, K., et al., High-performance bulk thermoelectrics with all-scale hierarchical architectures. *Nature*, 2012. **489**(7416): p. 414-418.
6. Androulakis, J., et al., High-temperature charge and thermal transport properties of the n-type thermoelectric material PbSe. *Physical Review B*, 2011. **84**(15).
7. Androulakis, J., et al., High-temperature thermoelectric properties of n-type PbSe doped with Ga, In, and Pb. *Physical Review B*, 2011. **83**(19).
8. Blum, I.D., et al., Dopant Distributions in PbTe-Based Thermoelectric Materials. *Journal of Electronic Materials*, 2012. **41**(6): p. 1583-1588.
9. Girard, S.N., et al., PbTe-PbSnS₂ thermoelectric composites: low lattice thermal conductivity from large microstructures. *Energy & Environmental Science*, 2012. **5**(9): p. 8716-8725.
10. He, J.Q., et al., Microstructure-Lattice Thermal Conductivity Correlation in Nanostructured PbTe_{0.7}S_{0.3} Thermoelectric Materials. *Advanced Functional Materials*, 2010. **20**(5): p. 764-772.
11. He, J.Q., et al., Strong Phonon Scattering by Layer Structured PbSnS₂ in PbTe Based Thermoelectric Materials. *Advanced Materials*, 2012. **24**(32): p. 4440-4444.
12. He, J.Q., et al., On the Origin of Increased Phonon Scattering in Nanostructured PbTe Based Thermoelectric Materials. *Journal of the American Chemical Society*, 2010. **132**(25): p. 8669-8675.
13. Lo, S.H., et al., Phonon Scattering and Thermal Conductivity in p-Type Nanostructured PbTe-BaTe Bulk Thermoelectric Materials. *Advanced Functional Materials*, 2012. **22**(24): p. 5175-5184.
14. Ohta, M., et al., Enhancement of Thermoelectric Figure of Merit by the Insertion of MgTe Nanostructures in p-type PbTe Doped with Na₂Te. *Advanced Energy Materials*, 2012. **2**(9): p. 1117-1123.

15. Zhao, L.D., et al., Raising the Thermoelectric Performance of p-Type PbS with Endotaxial Nanostructuring and Valence-Band Offset Engineering Using CdS and ZnS. *Journal of the American Chemical Society*, 2012. **134**(39): p. 16327-16336.
16. Zhao, L.D., et al., Thermoelectrics with Earth Abundant Elements: High Performance p-type PbS Nanostructured with SrS and CaS. *Journal of the American Chemical Society*, 2012. **134**(18): p. 7902-7912.
17. Liu, Y.F., et al., Large Enhancements of Thermopower and Carrier Mobility in Quantum Dot Engineered Bulk Semiconductors. *Journal of the American Chemical Society*, 2013. **135**(20): p. 7486-7495.
18. Makongo, J.P.A., et al., Simultaneous Large Enhancements in Thermopower and Electrical Conductivity of Bulk Nanostructured Half-Heusler Alloys. *Journal of the American Chemical Society*, 2011. **133**(46): p. 18843-18852.
19. Sahoo, P., et al., Enhancing thermopower and hole mobility in bulk p-type half-Heuslers using full-Heusler nanostructures. *Nanoscale*, 2013. **5**(19): p. 9419-9427.
20. Xie, W.J., et al., Significant ZT enhancement in p-type Ti(Co,Fe)Sb-InSb nanocomposites via a synergistic high-mobility electron injection, energy-filtering and boundary-scattering approach. *Acta Materialia*, 2013. **61**(6): p. 2087-2094.
21. Birkel, C.S., et al., Rapid Microwave Preparation of Thermoelectric TiNiSn and TiCoSb Half-Heusler Compounds. *Chemistry of Materials*, 2012. **24**(13): p. 2558-2565.
22. Birkel, C.S., et al., Improving the thermoelectric properties of half-Heusler TiNiSn through inclusion of a second full-Heusler phase: microwave preparation and spark plasma sintering of TiNi_{1+x}Sn. *Physical Chemistry Chemical Physics*, 2013. **15**(18): p. 6990-6997.
23. Sumithra, S., et al., Enhancement in Thermoelectric Figure of Merit in Nanostructured Bi₂Te₃ with Semimetal Nanoinclusions. *Advanced Energy Materials*, 2011. **1**(6): p. 1141-1147.
24. Douglas, J.E., et al., Enhanced thermoelectric properties of bulk TiNiSn via formation of a TiNi₂Sn second phase. *Applied Physics Letters*, 2012. **101**(18).
25. Misra, D.K., et al., Microstructure and Thermoelectric Properties of Mechanically Alloyed Zr_{0.5}Hf_{0.5}Ni_{0.8}Pd_{0.2}Sn_{0.99}Sb_{0.01}/WO₃ Half-Heusler Composites. *Science of Advanced Materials*, 2011. **3**(4): p. 607-614.
26. Zhao, L.D., et al., High Thermoelectric Performance via Hierarchical Compositionally Alloyed Nanostructures. *Journal of the American Chemical Society*, 2013. **135**(19): p. 7364-7370.
27. Takas, N.J., et al., Effects of Ir Substitution and Processing Conditions on Thermoelectric Performance of p-Type Zr_{0.5}Hf_{0.5}Co_{1-x}Ir_xSb_{0.99}Sn_{0.01} Half-Heusler Alloys. *Journal of Electronic Materials*, 2011. **40**(5): p. 662-669.
28. Makongo, J.P.A., et al., Thermal and electronic charge transport in bulk nanostructured Zr_{0.25}Hf_{0.75}NiSn composites with full-Heusler inclusions. *Journal of Solid State Chemistry*, 2011. **184**(11): p. 2948-2960.
29. Fistul, V.I., Heavily doped semiconductors. *American Journal of Physics*, 1969. **37**: p. 1291-1292.

Table of Contents Synopsis

Coherent full-Heusler nanoinclusions embedded in heavily-doped half-Heusler matrix induced large reduction in the thermal conductivity with constant power factor.

